Manuscript submitted to
AIMS' Journals
Volume **X**, Number **0X**, XX **200X**

doi:10.3934/xx.xx.xx.xx

pp. **X–XX**

4D-CT RECONSTRUCTION WITH UNIFIED SPATIAL-TEMPORAL PATCH-BASED REGULARIZATION

Daniil Kazantsev

The Manchester X-ray Imaging Facility, School of Materials, The University of Manchester
Manchester, M13 9PL, UK
Research Complex at Harwell
Didcot, Oxfordshire, OX11 0FA, UK

W. M. Thompson and W. R. B. Lionheart

School of Mathematics, The University of Manchester
Alan Turing Building, Manchester, M13 9PL, UK

G. Van Eyndhoven

iMinds-Vision Lab, The University of Antwerp
Wilrijk, B-2610, Belgium

A. P. Kaestner

Laboratory for Neutron Scattering and Imaging, Paul Scherrer Institut (PSI)
Villigen, 5232, Switzerland

K. J. Dobson and P. J. Withers and P. D. Lee

The Manchester X-ray Imaging Facility, School of Materials, The University of Manchester
Manchester, M13 9PL, UK
Research Complex at Harwell
Didcot, Oxfordshire, OX11 0FA, UK

Key words and phrases. time lapse tomography, spatial-temporal penalties, non local means, neutron tomography, GPU acceleration.

The first author is supported by EPSRC under the CCPi research grant EP/J010456/1.

Abstract. In this paper, we consider a limited data reconstruction problem for temporarily evolving computed tomography (CT), where some regions are static during the whole scan and some are dynamic (intensely or slowly changing). When motion occurs during a tomographic experiment one would like to minimize the number of projections used and reconstruct the image iteratively. To ensure stability of the iterative method spatial and temporal constraints are highly desirable. Here, we present a novel spatial-temporal regularization approach where all time frames are reconstructed collectively as a unified function of space and time. Our method has two main differences from the state-of-the-art spatial-temporal regularization methods. Firstly, all available temporal information is used to improve the spatial resolution of each time frame. Secondly, our method does not treat spatial and temporal penalty terms separately but rather unifies them in one regularization term. Additionally we optimize the temporal smoothing part of the method by considering the non-local patches which are most likely to belong to one intensity class. This modification significantly improves the signal-to-noise ratio of the reconstructed images and reduces computational time. The proposed approach is used in combination with golden ratio sampling of the projection data which allows one to find a better trade-off between temporal and spatial resolution scenarios.

1. **Introduction.** If one desires to improve the temporal resolution of a reconstructed dataset in order to reduce blurring from sample motion there is a need to either collect many projections quickly or to collect fewer projections. Further there are cases, for example when imaging living things, where there is a need to minimise the overall X-ray dose which can also lead to sparse temporal data. These strategies result in a low signal-to-noise ratio (SNR) of reconstructed images which are difficult to analyse and to segment. To increase the SNR and the resolution of images it is advisable to use iterative reconstruction techniques [1] over analytical methods (filtered back-projection (FBP) or Fourier direct inversion [2]).

In contrast to analytical methods, iterative approaches can accommodate: unconventional line integral, multiple acquisition models (mainly beneficial for emission tomography), different noise models (e.g. Poisson instead Gaussian statistics can be used to describe the photon counting process) and a priori information regarding the solution can be embedded into the reconstruction algorithm [3].

When dealing with underdetermined ill-posed problems in tomography it is necessary to impose additional constraints on the solution (e.g. smoothness) to ensure well-posedness of the inversion [3]. For example, smooth solutions are favoured more when applying the Tikhonov quadratic constraint (ℓ_2 norm minimization). The Tikhonov penalty is beneficial in noise suppression, however it also biases the solution significantly due to loss of the high frequencies (normally related to edges in the images). Penalties which approximate the ℓ_1 norm, such as total variation (TV) [4], can successfully deal with noise while leaving edges intact. Unfortunately these penalties lead to an undesirable "cartoon" effect when images are recovered as piecewise-constant valued regions. One can avoid the piecewise-constant appearance in reconstructed images, for example, by using higher order PDE's (e.g. fourth order) for the regularizing terms [5]. However, such techniques are local in the sense that they are based on the estimation of image gradients and usually very sensitive to the level of noise in the images.

Non-local (NL) image denoising methods [6] and regularization penalties based on them [7] have proven to be less sensitive to noise by considering similar neighbourhood patches (squared windows) in the image. Recently, a patch-based (PB)

regularization has been introduced which is equivalent to non-local penalties under certain assumptions [8, 9]. The PB regularization is presented as an optimization problem where different cost functions can be taken [8]. Some differences between PB and NL regularization methods are that for PB models there is: (a) the proposed cost function is independent on pre-estimated weights and therefore independent of the initial guess, (b) theoretical proof given for iterative NL means, (c) more flexibility for choosing various penalties. Using non-convex penalties for the cost function optimization can be beneficial for image quality, however it can lead to local minima (points). In this paper we use the relaxation or continuation strategy similar to [8] to improve the convergence properties of the iterative method using non-convex penalties in regularization.

In situations when series (time frames) of projection data are available it is beneficial to use temporal information in addition to spatial constraints [5],[10]-[18]. It is crucial to emphasize that the motion model is usually problem specific, therefore various model assumptions lead to different 4D reconstruction algorithms (a good overview can be found in [12]). Adding temporal information into the reconstruction using only adjacent time frames (*local*) is the "safest" method since it minimizes the risk of smoothing over distant time frames which potentially encompass significantly different information. Various techniques are used to penalize differences in adjacent time frames, such as, Gibbs smoothing [13], TV temporal penalty [16, 17], temporal higher order PDE smoothing [5] and non-local means [14, 10].

The local temporal regularization approach is well suited for experiments where significant motion is involved (which affects the region of interest (ROI)) during the scan (e.g. acyclic breathing of an unconscious patient) [17]. Using distant time frames in this case will cause strong artifacts in the reconstruction. However, in some cases when the motion is hard to predict and the dynamic changes happen within certain ROIs, the use of all time frames can significantly enhance the quality of the static objects [15, 18].

In this paper, we consider a dynamic imaging model, where some regions are static during the whole scan and some are dynamic (intensely or slowly changing) [19, 20]. Good example of such model is a movement of a fluid front (e.g. oil, water etc.) through a porous network (e.g. rock) [21]. The method we propose is closely related to the PB regularization in spatial and temporal domains [10]. The main difference from [10] is that all available time frames are used instead of only adjacent ones and an additional optimization strategy in the temporal domain is performed prior to the inter-patch calculations. The proposed combination is novel and leads to a substantial increase in resolution of time-repetitive features while minimizing the computational expense.

The majority of methods which use temporal information are local ones [12]. This is explained by the fact that in some applications the data changes quickly in time, therefore employing distant time frames will result in errors. Another aspect is that the computational time increases proportionally to the number of frames considered. Nevertheless, for certain applications the use of all time frames can be beneficial for the quality of the reconstructed images [5].

In this work we use ideas of Markov Random Field (MRF) probabilistic assumptions [22] to identify local structural correlations over multiple time frames. We aim to find the image structures (edges) which remain static in time, then based on the obtained structural information we perform temporal PB regularization. It is important that we minimize the number of patches in the temporal domain by

choosing elements of the image which belong only to the pre-built structural set. By calculating similarity measures between time independent patches we tend to minimize smoothing between structurally different elements.

This technique has the potential to significantly enhance edges which remain static during the acquisition scan while dynamic features normally remain smooth but are not eliminated. Additionally the proposed approach is able to decrease the number of aliasing artifacts. Furthermore, strong reduction of computational resources compared to other PB spatio-temporal methods [10] is provided with the proposed technique.

We use a splitting technique [23] to minimize a cost function in an alternating manner by switching between minimization of two sub-problems [8],[18],[16],[5]. The first step is performed with a conjugate gradient least squares (CGLS) optimization algorithm [25]; the second step is a fixed point iteration which includes the PB spatial-temporal smoothing term.

Four different numerical experiments (noisy image sequence recovery, synthetic modified Shepp-Logan phantom reconstruction, modelled fluid flow through rock and real data reconstruction) with visual and quantitative assessments were performed to evaluate the proposed approach. We perform a comparison of our method patch-based spatial-temporal MRF (PB-ST-MRF) with other state-of-the-art regularization techniques, namely: PB with spatial regularization (PB-S) [8] and PB spatial-temporal regularization (PB-ST) [10]. To further test our method we use neutron tomography (nCT) data to reconstruct dynamic aqueous flow through pore structures in rocks [21]. The very limited number of noisy projections (due to long exposures in nCT) and random artifacts makes it a good application to examine how effective the proposed method is.

The paper is organized as follows. In section 2, the methods are described for the parallel beam tomography model in 4D, the NL and PB regularization strategies are explained, the new MRF based spatial-temporal penalty and the proposed algorithm are presented. Section 3 shows numerical experiments of image sequences recovery, the reconstruction of two different synthetic dynamic phantoms and quantitative assessment for various methods. In addition the real data nCT experiment is shown. The results are discussed in section 4 and conclusions are drawn in section 5.

2. METHOD.

2.1. Parallel beam tomography model in 4D.

A discrete representation of the attenuation to be reconstructed can be written as a system of linear equations:

$$b_j = \sum_{i=1}^{\mathrm{N}} a_{ji} x_i + \delta_j, \tag{1}$$

where $b_j, j = 1, \ldots, \mathrm{M}$ is the measured projection data (sinogram), $x_i, i = 1, \ldots, \mathrm{N}$ is the discrete distribution of attenuation coefficient to be reconstructed and δ_j is the noise component in the measurements b_j. Weights $a_{ji} \in [0, 1]$ (contribution of element i to the value detected in the bin j) are forming the sparse system matrix $A : \mathbb{R}^{\mathrm{N}} \to \mathbb{R}^{\mathrm{M}}$.

Writing equation (1) in a matrix-vector form and adding the temporal dimension gives

$$\boldsymbol{b}_k = A_k \boldsymbol{x}_k + \boldsymbol{\delta}_k, \quad k = 1, 2, \ldots, K \tag{2}$$

where K is the total number of 3D time frames.

The explicit (direct) solution for (2) can be written as $\hat{\boldsymbol{x}_k} = A_k^\dagger \boldsymbol{b}_k$ with a pseudo-inverse $A_k^\dagger = (A^T A)_k^{-1} A_k^T \boldsymbol{b}_k$. This direct inversion (if practically possible) is highly sensitive to noise due to amplification of high-frequency components: $\hat{\boldsymbol{x}}_k = A_k^\dagger \boldsymbol{b}_k = A_k^\dagger (A_k \boldsymbol{x}_k + \boldsymbol{\delta}_k) = \boldsymbol{x}_k + A_k^\dagger \boldsymbol{\delta}_k$. In our case the system of equations (2) is severely underdetermined (M $\ll$ N) and the system matrix A is ill-conditioned. To find an approximate solution $\hat{\boldsymbol{x}}_k$ from the undersampled noisy measurements one can choose iterative techniques instead of conventional direct approaches [1, 3, 11].

Here we aim to reconstruct iteratively the unknown set of images $\boldsymbol{x}_k$ while adding a regularizing penalty in the spatial and temporal domain.

2.2. **Main structure of the 4D reconstruction algorithm.** Let us define $\boldsymbol{X} = (\boldsymbol{x}_1^T, \boldsymbol{x}_2^T, \ldots, \boldsymbol{x}_K^T)^T$ as the vector of all image time frames and similarly define the measured projections vector as $\boldsymbol{B} = (\boldsymbol{b}_1^T, \boldsymbol{b}_2^T, \ldots, \boldsymbol{b}_K^T)^T$. Therefore the system of equations to solve is $\boldsymbol{B} = \boldsymbol{A}\boldsymbol{X}$, where the block diagonal matrix $\boldsymbol{A}$ is given as:

$$\boldsymbol{A} = \begin{bmatrix} A_1 & 0 & \ldots & 0 \\ 0 & A_2 & & 0 \\ \vdots & & \ddots & \vdots \\ 0 & 0 & \ldots & A_K \end{bmatrix} \tag{3}$$

The traditional approach to solve a linear system of equations, such as (1), is to find the best fit $\hat{\boldsymbol{X}}$ to the exact $\boldsymbol{X}$ using a least-square approximation [1]. In other words, one would like to minimize the ℓ_2 norm between the forward projections and the projection data

$$\hat{\boldsymbol{X}} = \arg\min_{\boldsymbol{X}} \underbrace{\left\{ \frac{1}{2} \|\boldsymbol{A}\boldsymbol{X} - \boldsymbol{B}\|_2^2 \right\}}_{\Phi(\boldsymbol{X})}. \tag{4}$$

Since the cost function $\Phi(\boldsymbol{X})$ is quadratic, one can use gradient based approaches to find the minima of (4) by iteratively solving

$$\boldsymbol{X}^{n+1} = \boldsymbol{X}^n - \gamma \nabla \Phi(\boldsymbol{X}). \tag{5}$$

One can substitute $\nabla \Phi(\boldsymbol{X}) = \boldsymbol{A}^T(\boldsymbol{A}\boldsymbol{X} - \boldsymbol{B})$ into (5) to get the Landweber method [1]. This method converges iteratively to the least-squares solution with initialization $\boldsymbol{X}^0 = \boldsymbol{0}$ provided that $0 < \gamma < 2/\lambda_{max}$ where λ_{max} is the largest eigenvalue of $\boldsymbol{A}^T\boldsymbol{A}$. However, the speed of convergence for the Landweber method is slow (higher frequencies are recovered more slowly than the lower ones). In this work, we use the conjugate gradient least squares (CGLS) algorithm [25] to accelerate convergence and remove the need to identify the parameter γ empirically (5).

Unfortunately, even with faster optimization methods, such as CGLS, the solution for (4) is not uniquely defined due to noise and an ill-conditioned matrix $\boldsymbol{A}$. To turn (4) into a well-posed problem, one has to *regularize* the solution $\boldsymbol{X}$ by adding the *penalty* term $R(\boldsymbol{X})$, resulting in the following regularized problem:

$$\hat{\boldsymbol{X}} = \arg\min_{\boldsymbol{X}} \left\{ \frac{1}{2} \|\boldsymbol{A}\boldsymbol{X} - \boldsymbol{B}\|_2^2 + \beta R(\boldsymbol{X}) \right\}, \tag{6}$$

where β is a regularization parameter which represents the trade-off between the data fidelity and the regularization term.

The nature of the penalty $R(\boldsymbol{X})$ defines the strategy to minimize (6). If $R(\boldsymbol{X})$ is convex and differentiable (e.g. quadratic $R(\boldsymbol{X}) = \frac{1}{2}\|\Gamma\boldsymbol{X}\|_2^2$, where Γ is a linear

operator, such as a differential operator $\Gamma = \nabla$), the gradient based algorithms (5) can be used. In the case when $R(\boldsymbol{X}) = \|\Gamma \boldsymbol{X}\|_1$ the problem becomes non-differentiable and either approximations to ℓ_1 can be used [4] or other than gradient based techniques employed [23]. Non-convex penalties, e.g. $R(\boldsymbol{X}) = \|\Gamma \boldsymbol{X}\|_0$ can be strongly beneficial for the sparse signals, however, to avoid local minima more complicated optimization techniques should be used, e.g. simulated annealing [22].

Non-smooth penalties, such as total variation (TV) [4] have proven to be very effective by non-linearly penalizing local outliers in the image. Piecewise constant noiseless images can be obtained using the penalty $R(\boldsymbol{X}) = \|\nabla \boldsymbol{X}\|_1$. In contrast to a local gradient based regularizer, such as TV, we use a non-local regularizer which is related to non-local means [6].

2.3. **Non-local means for the spatial regularization.** Behind the NL means denoising technique proposed in [6] there is a simple idea of exploring image redundancy by averaging among similar patches. Instead of comparing intensity levels for different image pixels, which is an erroneous technique for noisy images, one can compare the subsets of pixels within squared window (patches). This approach is much more robust against noise.

Let $u : \Omega \to \mathbb{R}$ be a noisy image, then the noiseless approximation $\hat{u}$ can be obtained by NL averaging between patches in u as:

$$\hat{u} = \sum_{i \in \Omega} \sum_{j \in \mathcal{N}(i)} \omega_{ij} u_j, \tag{7}$$

where $\mathcal{N}$ is a *search window* with dimensions $(2\mathcal{N}_s + 1) \times (2\mathcal{N}_s + 1)$, and ω_{ij} is a weight between *similarity patches* $\mathcal{P}(u_i), \mathcal{P}(u_j)$ with dimensions $(2\mathcal{N}_p+1)\times(2\mathcal{N}_p+1)$ centred at points i and j respectively:

$$\omega_{ij} = \frac{1}{Z_i} \exp^{-\frac{\|\mathcal{P}(u_i) - \mathcal{P}(u_j)\|_\eta^2}{h^2}}, \tag{8}$$

where h is a filtering parameter, $Z_i = \sum_{j \in \mathcal{N}} \omega_{ij}$ is a normalization constant and η is a Gaussian function which gives more weight to the central element.

With a proper choice of the parameter h, the patches in u which are found to be similar in terms of the ℓ_2 metric will be averaged with higher weights ω. Dissimilar patches will be weighted less, however they still contribute to the final estimation of $\hat{u}$. Therefore the search window $\mathcal{N}$ should be large but not too large to avoid smoothing across many dissimilar patches (this leads to more blurry images). The size of the searching patch $\mathcal{P}$ is also an important parameter, and it is normally chosen according to the noise level in u. Additionally, the sizes of the search windows and similarity patches dictate the computational complexity of the algorithm [6].

For the non-local regularization of (6), one can employ the following penalty term [7]:

$$R(\boldsymbol{x}_k) = \sum_{i=1}^{N} \sum_{j \in \mathcal{N}(i)} \omega_{ij,k} (x_{i,k} - x_{j,k})^2, \quad k = 1, 2, \ldots, K \tag{9}$$

where spatial regularization of each time frame $\boldsymbol{x}_k = (x_{i,k})_{i=1,\ldots,N}$ depends on the pre-specified NL weights (8). Note that the weight $\omega_{ij,k}$ is calculated between i and j for the particular time frame k. The main problem of penalties such as (9) is the dependency of cost function on pre-specified weights ω_{ij}. In some cases a good initialization for x to estimate ω_{ij} might not be available.

Recently, a unified PB regularization penalty has been introduced [8] which is independent on a priory selected weights:

$$R(\boldsymbol{x}_k) = \sum_{i=1}^{N} \sum_{j \in \mathcal{N}(i)} \phi(\|\mathcal{P}(x_{i,k}) - \mathcal{P}(x_{j,k})\|_\eta), \quad k = 1, 2, \ldots, K \tag{10}$$

where $\phi : \mathbb{R} \to \mathbb{R}$ is a robust distance metric for non-linear weighting between patches. In [8] the term (10) was modified into:

$$R_{PB-S}(\boldsymbol{x}_k) = \sum_{i=1}^{N} \sum_{j \in \mathcal{N}(i)} \gamma_{ij,k}(\boldsymbol{x_k}) |x_{i,k} - x_{j,k}|^2, \quad k = 1, 2, \ldots, K \tag{11}$$

$$\gamma_{ij,k}(\boldsymbol{x_k}) = \sum_{\boldsymbol{p} \in \mathcal{B}} \eta(\boldsymbol{p}) \varpi_{(i-\boldsymbol{p}, j-\boldsymbol{p})}(\boldsymbol{x_k}); \ \boldsymbol{p} \in \underbrace{[-\mathcal{N}_p, \ldots, \mathcal{N}_p] \times [-\mathcal{N}_p, \ldots, \mathcal{N}_p]}_{\mathcal{B}}, \tag{12}$$

and

$$\varpi_{ij} = \psi(\|\mathcal{P}(x_i) - \mathcal{P}(x_j)\|_\eta), \tag{13}$$

where $\psi(x) = \phi'(x)/2x$ is a weight function. The significant difference between the model (11) and (9) is that the weights $\gamma(\boldsymbol{x_k})$ are obtained as the sum of similarity measures ϖ between all patch pairs in the search window $\mathcal{N}$.

It has been shown in [8] that the PB model (11) is equivalent to (9) under a proper choice of the function ϕ. For example one can see the similarity to (8) with:

$$\phi(x) = \left(1 - \exp(-x^2/h^2)\right); \quad \psi(x) = \exp(-x^2/2h^2). \tag{14}$$

Other types of $\phi(x)$ functions are given in [8], each producing slightly different results, but in this work we use functions given in (14).

As it is presented now, the term (11) introduces PB spatial regularization (PB-S) into problem (6), however at this stage the temporal dimension has not been considered. One can generalize the penalty term (11) to include temporal information and obtain some improvements.

2.4. **Temporal redundancy.** In [10], the problem of penalized image reconstruction from undersampled Fourier data for MRI application has been considered. The PB temporal regularization has been introduced by adding another dimension to the problem, in other words, dynamic 2D data was tackled as a 3D volume, where the third coordinate is time (k). In particular, for the penalty in (11), the search window was taken as $\mathcal{N} = \mathcal{N}_{s,x} \times \mathcal{N}_{s,y} \times \mathcal{N}_{s,k}$ and the similarity patch $\mathcal{P} = \mathcal{N}_{p,x} \times \mathcal{N}_{p,y} \times \mathcal{N}_{p,k}$. The size of the temporal dimension (the number of time frames included) $\mathcal{N}_{s,k}$ was set to 5 and $\mathcal{N}_{p,k} = 3$. We refer to this approach as the PB spatial-temporal technique (PB-ST).

Here we present a novel idea where all the available temporal data is used to improve the resolution of correlated structures even further. We unify the spatial and temporal approaches into one penalty term. However, patches in the temporal space will be treated differently from patches in the local time frame. Since only certain patches in the temporal space are taken into account, the computational performance of the proposed technique is significantly faster in comparison to the PB-ST method [10]. Furthermore, the proposed approach yields better SNR values for the reconstructed images.

Following ideas from [10], the penalty term (11) can be generalized for all temporal frames to be included with $\mathcal{N}_{s,k} = K$. However, due to the large number of potentially different time frames within the search window ($\mathcal{N} = \mathcal{N}_{s,x} \times \mathcal{N}_{s,y} \times K$),

the denoising procedure might be prone to oversmoothing and infeasibly slow to compute.

Our novel idea is to minimize the amount of temporal information by taking into account only the most probable patches within the window $\mathcal{N} = \mathcal{N}_{s,x} \times \mathcal{N}_{s,y} \times K$. To identify those patches we use ideas based on Markov random fields (MRF) for natural images [22]. The Gibbs assumption on the distribution of pixels in noiseless images claims that closer neighbours to the central pixel have the highest probability to be within one intensity class [24]. One can use a simple absolute difference metric to find the most similar neighbours. This metric, however, is very sensitive to noise in images, therefore, to ensure improved stability, we propose to calculate it globally across multiple time frames.

The proposed unified spatial-temporal penalty is defined as follows:

$$R_{PB-ST-MRF}(\boldsymbol{x}_k) = \sum_{i=1}^{N} \Bigg[\underbrace{\sum_{j \in \mathcal{N}(i)} \gamma_{ij,k}(\boldsymbol{x}_k)|x_{i,k} - x_{j,k}|^2}_{\text{Spatial}} + \underbrace{\sum_{l \in \{1,2,\ldots,K\} \setminus \{k\}} \sum_{j \in \aleph_K(i,n_0,S)} \gamma_{ij,l}(\boldsymbol{x}_l)|x_{i,k} - x_{j,l}|^2}_{\text{Temporal}} \Bigg], \quad k = 1,2,\ldots,K \tag{15}$$

The regularization term (15) consists of the spatial part which is exactly the same as (11) and the temporal part which depends on the pre-specified set $\aleph_K(i, n_0, S)$. Now we explain how the set $\aleph_K(i, n_0, S)$ is defined for every element i.

In Fig. 1 we show how the set $\aleph_K(i, n_0, S)$ can be identified for the number of time frames $K = 3$. This example demonstrates the 3D problem (2D $(x, y$ coordinates) + 1D (time)), although it can be easily generalized to 4D. We call $\aleph_K(i, n_0, S)$ the *structural set*, since it represents the most probable (in the sense of Gibbs notion) distribution of correlated structured features (e.g. edges) across all time frames in the searching window S. Initially, the generalized map is formed by a linear projection of the similarity measures (absolute differences) for every neighbour j, calculated in every time frame, on a imaginary space (depicted as a bottom layer in Fig. 1, left). Then, the n_0 number of the most prominent neighbours is chosen to build the structural set $\aleph_K(i, n_0, S)$ (depicted as a bottom layer in Fig. 1, right). Finally, the weights are calculated only for the elements of the selected set $\aleph_K(i, n_0, S)$ (temporal part of the term (15)).

Selection of the most prominent neighbours (total number n_0) is performed according to the following thresholding principle:

$$P_1 \leq \cdots \leq P_{n_0} \leq \cdots \leq P_n; \quad n = 1, \ldots, |S(i)| \tag{16}$$

where $P_n = \sum_{k=1}^{K} |u_{i,k} - u_{j_n,k}|$, and $|S(i)|$ is a total number of neighbours in the searching window (e.g. for $S = 3$ in 3D, $|S(i)| = S \times S \times S - 1 = 26$ neighbours). The threshold value P_{n_0} can be specified by assigning n_0 to some constant value and usually n_0 is taken to be $25 - 30\%$ of $|S(i)|$ (e.g. $n_0 = 9$ for $|S(i)| = 26$).

When the structural set is found $\aleph_K(i, n_0, S)$ (see Fig. 1, right) one can perform the calculation of PB weights (12) with every selected element (neighbour) in the

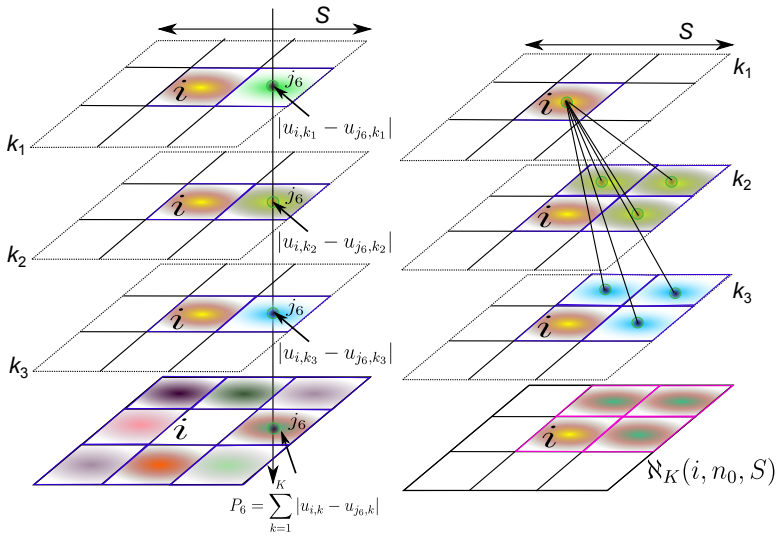

FIGURE 1. 3D representation (2D (x, y dimensions) + 1D (time)) of the structural set $\aleph_K(i, n_0, S)$ which is build from all available time frames K (here $k_{1,2,3}$). For every time frame the absolute differences are calculated and then summed over all time frames resulting in the generalized map (bottom layer in left image). The resulting generalized map of all absolute differences is analysed and certain neighbours (total amount of n_0) are taken into the set $\aleph_K(i, n_0, S)$ (bottom layer in right image). Then for each element i, the set $\aleph_K(i, n_0, S)$ is used to choose elements for the PB regularization in the temporal space only. On the right image the weights are calculated with respect to the time frame k_1.

other time frames. Note that for the current time frame (k_1 on Fig. 1, right) the MRF-based set $\aleph_K(i, n_0, S)$ is not used but the classical spatial PB regularization is performed (15).

The main idea of the following approach is to minimize the number of candidates in the temporal domain for calculating non-local weights. If some structural boundaries are present through time they will be further enhanced since all irrelevant (dissimilar) neighbours are not considered.

Therefore the proposed PB-ST-MRF technique uses only $\mathcal{N}_{s,x}\mathcal{N}_{s,y}\mathcal{N}_{s,z} + P_{n_0}K + K$ elements instead $\mathcal{N}_{s,x}\mathcal{N}_{s,y}\mathcal{N}_{s,z}K$ for PB-ST method. Our modification significantly reduces the number of computations and increases the resolution of the images.

2.5. **Numerical algorithm.** In this section we present an efficient way to solve (6) with the proposed penalty (15). Following [8] we split our minimization problem into two subproblems. The first problem is the least squares minimization (4) which we solve with the CGLS algorithm [25]. And the second problem includes the proposed penalty term (15):

$$\arg\min_{\boldsymbol{x}_k} \|\boldsymbol{x}_k - \hat{\boldsymbol{x}}_k\|_2^2 + \beta R_{PB-ST-MRF}(\boldsymbol{x}_k), \;\; k = 1, 2, \ldots, K \tag{17}$$

where $\hat{\boldsymbol{x}}_k$ is initialized with a solution from CGLS step. Note that for PB-ST-MRF penalty (15) all time frames K should be reconstructed prior to the step (17).

The problem (17) is solved with one (though many iterations are possible) fixed point step [8]:

$$\boldsymbol{x}_k^{n+1} = \frac{\hat{\boldsymbol{x}}_k + \frac{\beta}{2}\left[\sum_{j\in\mathcal{N}(i)} \gamma_{ij,k}(\hat{\boldsymbol{x}}_k)\hat{x}_{j,k} + \sum_{l\in\{1,2,\ldots,K\}\setminus\{k\}} \sum_{j\in\aleph_K(i,n_0,S)} \gamma_{ij,l}(\hat{\boldsymbol{x}}_l)\hat{x}_{j,l}\right]}{1 + \frac{\beta}{2}\left[\sum_{j\in\mathcal{N}(i)} \gamma_{ij,k}(\hat{\boldsymbol{x}}_k) + \sum_{l\in\{1,2,\ldots,K\}\setminus\{k\}} \sum_{j\in\aleph_K(i,n_0,S)} \gamma_{ij,l}(\hat{\boldsymbol{x}}_l)\right]} \tag{18}$$

The pseudocode of our reconstruction method is given in Algorithm 1. The regularization methods used in this paper were implemented in C with open multi-processing (OMP) support and CUDA languages to parallelize and accelerate computations. The open source codes are freely available through the following link [28].

Algorithm 1 Simultaneous 4D reconstruction with unified PB-ST-MRF regularization and continuation strategy

Initialize: $\boldsymbol{X} = \boldsymbol{0}$, N (iterations number), β, $\mathcal{N}_s$, $\mathcal{N}_p$, h_{fixed}, h_{fac}, n_0, S

$h = h_{\text{fixed}} + Nh_{\text{fac}}$;

while $n < N$ **do**

- perform one iteration of CGLS to get estimate $\hat{\boldsymbol{X}}$
- perform fixed point step (18) using h in $\gamma_{ij,k}(\hat{\boldsymbol{x}}_k)$ estimation and h_{fixed} in $\gamma_{ij,l}(\hat{\boldsymbol{x}}_l)$ estimation
- check convergence criteria; if stop return $\boldsymbol{X}^{n+1}$
- $h = h - Nh_{\text{fac}}$;
- $n = n + 1$;

end

return $\boldsymbol{X}^{n+1}$

Using non-convex penalties with (13) can be beneficial in improved resolution of images, however the optimization problem becomes more challenging [8]. Local minima might be present and to avoid convergence to them there are effective but highly computationally expensive methods, such as simulated annealing [22]. In [8], the continuation strategy is used to improve convergence, however location the global minima is not guaranteed. The main idea is to relax parameter h by taking it larger on the first iterations of algorithm and then reducing its value in iterations. This leads to isotropic smoothing of noise on the first iterations and then non-isotropic treatment of image structures on higher iterations. In practice this technique works quite well and it also very simple to implement.

In our algorithm we perform this strategy for the spatial part of the regularization term (15) but keep h fixed for the the temporal part (to avoid larger weights in-between different time frames). The factor h_{fac} is chosen to be a small constant. For our experiments we used the number of iterations as a stopping criteria for iterative process, however other stopping rules can be used [1].

3. **Numerical Experiments.** In this section we perform four different numerical experiments to demonstrate the feasibility and the improvement of the proposed technique over current state-of-the-art methods. The first experiment presents an image sequence denoising problem. We compare three denoising algorithms which all use the PB model to restore the noisy image. The second and third experiments demonstrate the 2D tomographic reconstruction of dynamically changing phantoms and the fourth one considers a dynamic reconstruction of neutron data. For parallel projection and backprojection operations we used GPU accelerated modules from the ASTRA toolbox [31].

In the following experiments we use a non-convex function ϕ (14). The algorithms differ in the way the temporal information is handled. The BP-S method performs only spatial denoising [8], the BP-ST method treats the 2D sequence of images as 3D data (adjacent time frames are taken only) [10]. The proposed method BP-ST-MRF (15) uses all available image sequences, however the amount of temporal information is significantly reduced with the MRF approach (see section 2.4).

3.1. **Image sequence denoising experiment.** Here we demonstrate an example of denoising a sequence of noisy images (video denoising). The noiseless image "Lena" was taken (see Fig. 2 (a)) and 25 realizations of normal noise (with standard deviation of 10% of the signal) have been applied resulting in 25 images with randomly distributed noise (see the first image from the sequence on Fig. 2 (b)).

To quantify our results we use the signal-to-noise ratio (SNR) metric in decibels (dB):

$$SNR(u, u^*)_{ROI} = 20 \log \left(\frac{\|u\|_2}{\|u - u^*\|_2} \right), \tag{19}$$

where u is the ideal image and u^* is a recovered one.

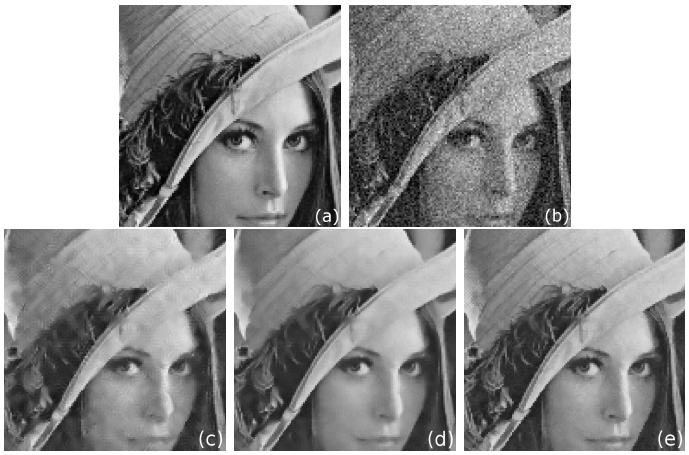

FIGURE 2. Image sequence denoising experiment. (a) original noiseless image (magnified part), the original image has 256×256 pixels size; (b) a noisy image; (c) PB-S; (d) PB-ST; (e) PB-ST-MRF. Images obtained with the following parameters: $\mathcal{N}_s = 5, \mathcal{N}_p = 3, h = 0.2, \beta = 0.1, n_0 = 3, S = 3$.

We empirically tested each of the methods for the optimal set of parameters to achieve the best SNR values which are provided in table 1. The spatial denoising

with PB-S method gives the lowest SNR and strong artifacts are visible on the images (see Fig. 2 (c)). By including adjacent image sequences with PB-ST method one can reduce the number of artifacts, improve image resolution and increase the SNR. Using all available image sequences with the PB-ST-MRF method we significantly improve resolution (note how some features are better resolved, e.g. the hat, nose) and it gives the best SNR level.

TABLE 1. Image sequence denoising experiment illustrated in Fig. 2, SNR (19) and computation times for the various methods

	u_{noise}	PB-S	PB-ST	PB-ST-MRF
SNR/dB	15.32	22.6	25.8	28.2
Time/sec		10.1	510.2	25.9

In table 1, the computation times for all algorithms on 8 cores Intel Xeon CPU 2.27GHz are provided. The times given in the table represent the recovery of all 25 image sequences. The computer codes (C and CUDA versions) which reproduce the presented example are freely available through the following link [28]. The computational time strongly depends on the size of the searching window and the similarity patch. With the number of image sequences the computational time increases drastically (see the time for PB-ST method). For 4D data with higher resolution the computational time for PB-ST method becomes impractical. The proposed reduction technique within the PB-ST-MRF method (see section 2.4) can significantly reduce the computation time. The GPU acceleration of the algorithm further reduces time of computation.

3.2. **Golden ratio firing order.** For the more realistic modelling of our reconstruction experiment using a synthetic phantom we used a Golden ratio (GR) scanning angle decomposition strategy [29, 30]. This firing technique is used in practice [20] providing a flexible image acquisition strategy for dealing with motion related experiments [29]. Since the real data results considered in this paper were obtained using GR acquisition, it is more consistent to use this firing technique for the synthetic data as well.

The GR scanning approach [30] is used to obtain projections in a non-sequential order. The basic idea is to adapt the angle sequence of projections so that any subsets of chronologically contiguous projections contain sufficient information for reconstruction [29]. This technique is well suited to iterative reconstruction methods when one can divide the scan into an arbitrary number of subscans which are normally sampled below the Nyquist rate.

The method uses the GR constant $\chi = (1 + \sqrt{5})/2$ to determine the next projection angle. In this scheme, the acquisition angle θ of i projection is described by

$$\theta_i = i\chi\pi \bmod \pi, \tag{20}$$

therefore two consequent projections taken with (20) will be nearly orthogonal to each other. Every subsequence of the whole projection set covers the scan arc from π to 2π. This is an important feature for the ability to reconstruct the data with different spatiotemporal resolutions. This acquisition scheme can be started with no predefined end and arbitrarily terminated at any convenient end point [29].

3.3. **Dynamic 2D Shepp-Logan (SL) phantom reconstruction.** In this section we present numerical results for the reconstruction of an idealised 3D phantom (x, y spatial coordinates and time k).

In Fig. 3 (a), the 3D synthetic phantom for the numerical experiments is presented. The spatial x, y dimensions are 128×128 pixels and the temporal dimension is $K = 64$ (z dimension in the volume shown in Fig. 3 (a)). The phantom comprises several static objects which remain stationary during the experiment (objects without numbers in Fig. 3 (a)) as well as objects 1-3. The presented objects have different intensity values. We test our method by introducing 64 frames during which object 1 is shifting, object 2 is rotating and object 3 is contracting (see Fig. 3 (b-d)).

We performed a forward projection of 2D $\boldsymbol{x}_k$ phantoms ($k = 1, 2, \ldots, K$) using 160 detectors and 30 acquisition angles per time frame. Note that the 30 angles were distributed over a $[0, \pi]$ angular interval using the GR strategy (20) and we assume that the whole object is stationary during each time frame. Then δ_k realizations of Poisson noise were applied to the data assuming an incoming beam intensity of 5000 photon counts per detector pixel. Using noisy sinograms $\boldsymbol{b}_k$, all phantoms were reconstructed using the CGLS method [25], PB-S, PB-ST, PB-ST-MRF methods (see Fig. 4). To demonstrate how temporal resolution can be easily lost we reconstructed the whole set $\boldsymbol{b}_k$ using FBP [2] as a single sinogram (see Fig. 3 (e)).

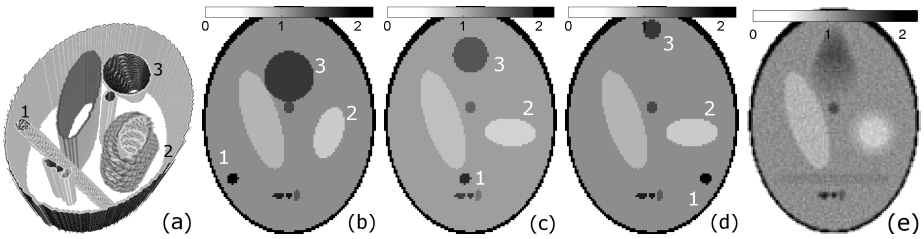

FIGURE 3. 3D phantom with spatial dimensions 128×128 pixels and $K = 64$ time frames during which 30 projections were acquired for each. It comprises of several static objects (no numbers) and dynamic objects (1-3). Object 1 moves from the left to the right, object 2 quickly rotates anticlockwise around its own axis and object 3 contracts. One can visualise the time series as a 3D rendered volume (a). Slices 1 (b), 30 (c) and 64 (d) are shown. In (e), the FBP reconstruction of all time frames forming one sinogram (size of 160×1920 pixels) is presented. Note the loss of temporal resolution and the significant noise level.

TABLE 2. Dynamic SL reconstruction experiment, SNR (19) values for the various methods illustrated in Fig. 4.

	FBP	CGLS	PB-S	PB-ST	PB-ST-MRF
Static ROI's	12.4	15.1	23.6	25.4	29.0
Dynamic ROI's	16.3	19.0	22.1	24.3	22.2

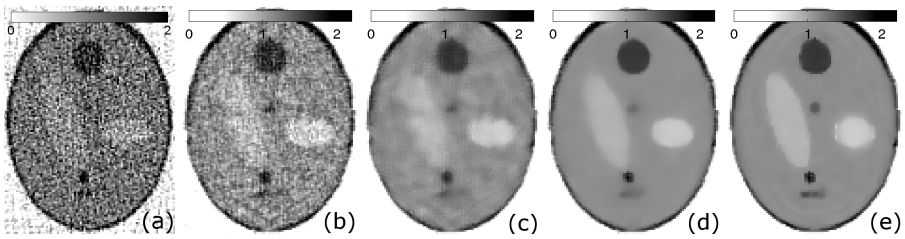

FIGURE 4. 2D reconstructions of frame No. 30 (see Fig. 3 (c)) reconstructed from 30 projection angles: FBP (a), CGLS (b), PB-S (c), BP-ST(d), BP-ST-MRF (e). The parameters used were (see Algorithm 1): $N = 10, \beta = 0.002, \mathcal{N}_s = 5, \mathcal{N}_p = 3, h_{\text{fixed}} = 0.1, h_{\text{fac}} = 0.01, n_0 = 3, S = 3$.

The reconstruction processes for FBP, CGLS, PB-S, PB-ST and BP-ST-MRF methods were optimized to the maximum of SNR values for each method. The SNR values were calculated for ROIs belonging to the static and dynamic objects and are summarized in table 2. As expected, for static objects the proposed method outperforms others, however for dynamic objects the PB-ST method gives slightly better results.

It can be noted that not all dynamic objects reconstructed with the PB-ST-MRF method are worse than with PB-ST. Notably object 2 (which has a fast and repetitive rotation cycle) is reconstructed more poorly (the loss of the elliptical shape) than the others with PB-ST-MRF. This is due to the fact that our MRF based method generalizes information about repetitive structures in time (see section 4). The PB-ST-MRF method is better suited to objects which are appearing and disappearing in time without any repetition, such as the object 1. Since the object 2 is contracting slowly in time our method brings certain artifacts which affect the shape of the circle. However it is not crucial and certainly not worse in resolution than PB-S. We can generalize by stating that the proposed method gives the same or better results for dynamic objects than the spatial based approach. However the recovery of the static objects is considerably better with the proposed method.

3.4. **Dynamic reconstruction of a simulated phantom modelling fluid flow through rock.** To further demonstrate the applicability of the PB-ST-MRF method, a more realistic phantom was designed.

The synthetic phantom was created as follows. First, a high quality reconstruction based on an X-ray projection data set of rock (porous granitic gravel), which was acquired on a Nikon XTH 225 ST scanner at the Manchester X-ray facility, was calculated with a Feldkamp algorithm. This reconstruction is displayed in Fig. 5(a). Based on this reconstruction, the rock region was extracted and all other attenuation values were set to zero, resulting in the image displayed in Fig. 5 (b). Next, fluid flow was simulated in the void space region, where the time points at which fluids enters a certain voxel were randomly generated by applying a global thresholding operation on a 2D Perlin noise image [26].

In total, 1500 projections using the GR firing order (20) were simulated. Each projection was generated with a strip kernel [2] and a higher resolution version of the phantom, i.e., on a 800×800 isotropic pixel grid. Poisson distributed noise was applied to the projection data, assuming an incoming beam intensity of 10000

(photon count). Reconstructions were calculated on a 200×200 isotropic pixel grid and with a linear projection model [2], thus avoiding the "inverse crime" of generating the data with the same model as the model that is used for calculating the reconstruction [27]. In total, 30 different time frames were reconstructed by subdividing the simulated projection data into 30 distinct subsets of 50 projections each.

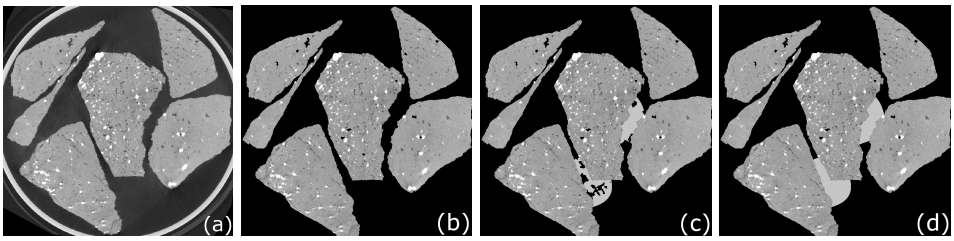

FIGURE 5. Reconstruction of the porous granitic gravel sample from 2000 projections using the Feldkamp algorithm (a); three different time frames of the resulting sequence of simulated images are displayed in (b-d)

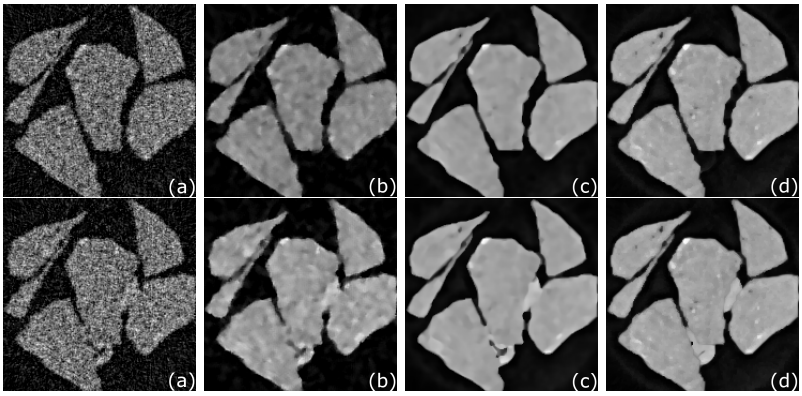

FIGURE 6. 2D reconstructions of the time frame $k = 1$ (top row) and $k = 18$ (bottom row) with methods CGLS (a), PB-S (b), BP-ST(c), BP-ST-MRF (d). The parameters used were (see Algorithm 1): $N = 10, \beta = 0.01, \mathcal{N}_s = 5, \mathcal{N}_p = 3, h_{\text{fixed}} = 20, h_{\text{fac}} = 1, n_0 = 3, S = 3$.

Similarly to the experiment in section 3.3, we calculated SNR values for the static (rock) and for dynamic (simulated fluid flow) ROIs (see table 3). The behaviour of the proposed method is very similar to the previous experiment. The static part of the phantom (rock) is reconstructed with very good resolution (see Fig. 6) and with higher SNR in comparison to all other methods. However, the reconstructed dynamic part with BP-ST-MRF method is slightly biased (oversmoothed) in comparison to the ground truth and the SNR value is lower than for BP-ST method. This drawback of the proposed technique is expected and several solutions to overcome this problem are given in section 4.

TABLE 3. Dynamic SL reconstruction experiment, SNR (19) values for methods

	CGLS	PB-S	PB-ST	PB-ST-MRF
Static ROI's	9.29	15.27	16.2	17.1
Dynamic ROI's	11.1	16.35	17.23	16.48

As indicated by the numerical results, our method performs better or worse depending on the specific class of the dynamic reconstruction problem. There is, however, a class of applications where our method consistently gives better results than the other methods.

3.5. **Reconstruction of neutron tomography data.** Neutron tomography (nCT), like x-ray tomography (xCT), is a non-destructive technique which can provide three-dimensional (3D) images from reconstruction of a series of 2D projections (radiographs). Unlike x-rays, neutrons interact with the atomic nuclei, and so materials with similar atomic numbers can have different attenuation cross sections. The two techniques are therefore often complementary, giving different information about the internal structure [19].

In this study we exploit the high attenuation of neutrons by hydrogen to locate water rivulets within a rock volume (see Fig. 7). Aqueous fluids are very difficult to observe using x-rays due to their low attenuation compared to rock, therefore nCT can be helpful in this case, but because neutron fluxes are typically much lower than x-ray fluxes neutron images of temporally varying systems are often very noisy.

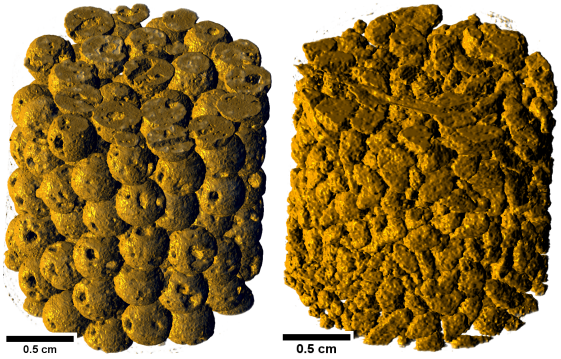

FIGURE 7. left: basalt rock beads inside a neutron transparent aluminium container, reconstructed using CGLS-PBS algorithm; right: sandstone rock beads with finer porosity (10-20%) and a different type of pore geometries to basalt.

The experiment was performed on the cold neutron imaging Beamline ICON at SINQ spallation neutron source at Paul Scherrer Institute, Switzerland [20]. A packed set of porous rock beads (see Fig. 7) (basalt with 4 mm diameter and sandstone with 1mm in a middle section) was loaded into a 25 mm thin walled aluminium tube, and the sample holder mounted in a gravity driven flow cell. The flow cell was then mounted on a rotating stage in the essential parallel neutron

beam. A CCD camera was used to acquire images at different rotation angles according to the GR selection rule (20) with an exposure time of 20s per projection.

In nCT the spatial resolution available is generally worse than is possible with x-ray systems, the flux lower and nCT projections are more strongly influenced by a scattering contribution, making reconstructions significantly noisier than for xCT [20]. In this experiment, the signal to noise ratios are reduced by the short acquisition times for each frame and the reduced number of projections employed to try and capture the dynamic process. Therefore the measured data is ideally suited for the proposed spatial-temporal technique.

In this study we present reconstructions of rock samples in the absence (dry) and presence (wet) of aqueous flow though pore structures in the rocks (basalt and sandstone). In order to capture the dynamic propagation of water through the pores, it is necessary to use a limited number of projections and the use of iterative techniques for data reconstruction is essential. We employ FBP, CGLS, PB-S and PB-ST-MRF algorithms to reconstruct the data. The algorithm PB-ST is not used here.

To reconstruct basalt rock, only 80 projections per time frame were used with 1000×1000 pixels image size. The part of image which shows the dynamic fluid flow through basalt beads for different time frames is demonstrated on Fig. 8.

The proposed method provides a significant enhancement of SNR and resolution in reconstructed images while showing dynamic water ingress in time. The streak artifacts (due to damaged pixels in the projection data) are completly alleviated with the PB-ST-MRF method (see Fig. 8 (time step 2)). The improved quality of reconstructed images makes further quantitative analysis of geological features and water dynamics possible. We also present a few rendered images of the reconstructed sandstone sample (see Fig. 9) where changes in water distribution within the rock are clearly visible.

4. **DISCUSSION.**

Dynamic processes that require fast tomographic imaging [32], such as aqueous flow through geological samples, require the use of as few projections as possible per frame and a mechanism for dealing with low signal to noise ratio. Using adjacent time frames leads to better bias-noise characteristics, however, for certain experiments the use of all time frames can be more beneficial.

Normally, the static structures are not the main object of interest for the experimentalist, therefore inducing strong artifacts in the temporal domain can lead to biased quantifications. Even using non-linear measures, such as non-local weights, to penalize differences in-between time frames can lead to bias resolving spatial and temporal resolution.

Exploiting all time frames in the MRF based structural map (see section 2.4) can lead to oversmoothing effects in the dynamic regions. There are possible solutions to overcome this drawback of the method and this is the subject of our future research. One possible approach consists of reducing the weights or completely restrict the temporal PB averaging in the dynamic regions. To implement this approach, the static and dynamic parts of the object (e.g., rock and water, respectively) should be identified prior to the actual reconstruction. This identification can, for example, be achieved by acquiring *a priori* projections from the static object (i.e. before the dynamics initiated) and extracting the static/dynamic part from the corresponding static reconstruction. Furthermore, the dynamic event location can be identified

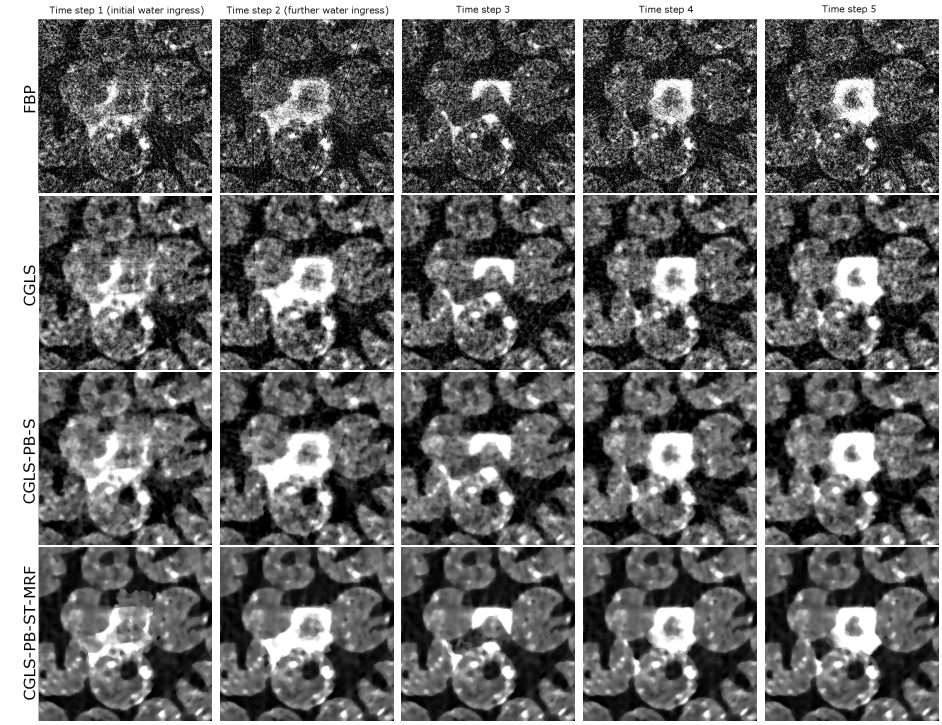

FIGURE 8. 2D slices of reconstructed 3D basalt sample using FBP, CGLS, PB-S, PB-ST-MRF methods. Each time frame (here k=1-5) was reconstructed from only 80 projections. Note the improved spatial resolution without loss of the temporal resolution and the absence of streak artifacts with PB-ST-MRF method. The parameters used were (see Algorithm 1): $N = 10, \beta = 0.023, \mathcal{N}_s = 5, \mathcal{N}_p = 3, h_{\text{fixed}} = 0.11, h_{\text{fac}} = 0.03, n_0 = 3, S = 3$.

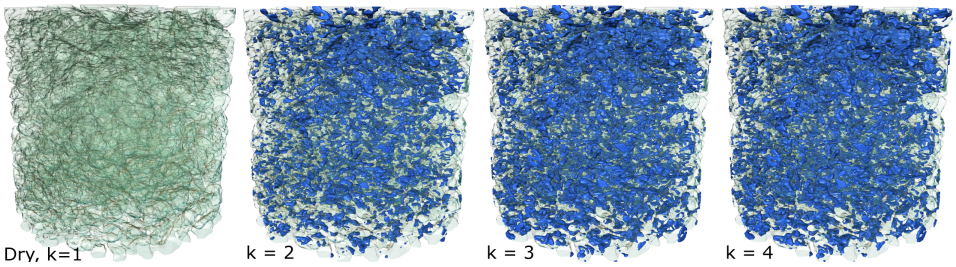

FIGURE 9. The reconstructed and rendered volumes of the sandstone sample (see Fig. 7, right) related to the different time states, the dry state (k = 1) is a reconstruction using 150 projections and subsequent 3 reconstructions of a wet stages are reconstructed from subsequent 100 projections.

automatically and this information can be exploited to apply some extra constraints, e.g. for restricting the set of time frames that is used in the temporal averaging.

Additionally, different weighting factors can be assigned to different time frames, based on *a priori* knowledge of the dynamic, resolution and noise characteristics of each specific frame (e.g., the number of projections is higher in one frame than in another frame).

Discontinuous scanning protocols, such as Golden ratio sampling is a sensible option for dynamic experiments. This scanning technique allows flexibility to investigate a range of time frame/spatial resolution scenarios to determine the most appropriate balance between temporal and spatial resolution [29].

For certain experimental problems the identification of the displacement field can help to embed the motion model in reconstruction. Unfortunately for the fluid flow problems the motion model is hard to describe due to its very random and discontinuous behaviour.

Increasing the number of time frames gives better SNR for the proposed method sacrificing the computational speed.

5. **CONCLUSION.** In this paper, we presented results of a spatial-temporal regularization technique which is based on non-local methods for image denoising. The novelty of the proposed penalty is in the unified and global nature of treating spatial and temporal information. Additionally, a new optimization strategy in the temporal domain is proposed, leading to a reduction of computation time and better resolution and noise characteristics of the reconstructed images.

Applying the proposed method to different synthetic phantoms resulted in better resolution and reduced noise in the reconstructed images. Additionally, the method was successfully applied to a 3D neutron tomography data set which has a limited amount of noisy projections. Obtained reconstructions showed good SNR and resolution characteristics. As such, this method has potential for application in the visualisation and quantification of dynamic processes.

Acknowledgments. This work has been supported by the Engineering and Physical Sciences Research Council under grants EP/J010456/1 and EP/I02249X/1. Travel was supported by the European Commission under the 7th Framework Programme through the "Research Infrastructures" action of the "Capacities" Programme, NMI3-II Grant No. 283883, Project No.20120553. Networking support was provided by the EXTREMA COST Action MP1207.

REFERENCES

[1] C. L. Byrne, *Applied Iterative Methods*, Natick, MA: Peters, 2008.

[2] A.C. Kak and M. Slaney, *Principles of computerized tomographic imaging*, IEEE Press, New York, 1998.

[3] J. Qi and R.M. Leahy Iterative reconstruction techniques in emission computed tomography, *Phys Med. Biol.*, **51** (2006), R541–R578.

[4] L.I. Rudin, S. Osher and E. Fatemi Nonlinear total variation based noise removal algorithms, *Physica D.*, **60** (1992), 259–268.

[5] D. Kazantsev, W.R.B. Lionheart, P.J. Withers and P.D. Lee GPU accelerated 4D-CT reconstruction using higher order PDE regularization in spatial and temporal domains, *In Proc. CMSSE* Almeria, Spain, **3** (2013), 843–852.

[6] A. Buades, B. Coll and J.M Morel A review of image denoising algorithms with a new one, *Society for Industrial & Applied Mathematics (SIAM)*, **4(2)** (2006), 490–530.

[7] S. Bougleux, G. Peyre and L. Cohen Non-local regularization of inverse problems, *American Institute of Mathematical Sciences (AIMS)*, **5(2)** (2011), 511–530.

[8] Z. Yang and M. Jacob Nonlocal regularization of inverse problems: a unified variational framework, *IEEE Trans. on Image Process.*, **22(8)** (2013), 3192–3203.
[9] G. Wang and J. Qi Penalized likelihood PET image reconstruction using patch-based edge-preserving regularization, *IEEE Transactions on Medical Imaging*, **31(12)** (2012), 2194–2204.
[10] Z. Yang and M. Jacob Robust non-local regularization framework for motion compensated dynamic imaging without explicit motion estimation, *2012 9th IEEE International Symposium on Biomedical Imaging (ISBI)*, (2012).
[11] D.S. Lalush and M.N. Wernick Iterative Image Reconstruction, in *Emission Tomography* eds. Mark T Madsen, Academic Press, 2004, 443-472.
[12] A. Rahmim, J. Tang and H.Zaidi Four-dimensional (4D) image reconstruction strategies in dynamic PET: Beyond conventional independent frame reconstruction, *Med. Phys.*, **36** (2009), 3654–3670.
[13] D.S. Lalush and B.M.W. Tsui Block-iterative techniques for fast 4D reconstruction using a priori motion models in gated cardiac SPECT, *Phys Med. Biol.*, **43** (1998), 875–886.
[14] X. Jia, Y. Lou, B. Dong, Z. Tian and S. Jiang 4D computed tomography reconstruction from few-projection data via temporal non-local regularization, in *Medical Image Computing and Computer-Assisted Intervention – MICCAI 2010*, Springer Science Business Media (2010), 143–150.
[15] G. Van Eyndhoven, K. J. Batenburg and J. Sijbers Region-Based Iterative Reconstruction of Structurally Changing Objects in CT, *IEEE Trans. on Image Process.*, **23(2)** (2014), 909–919.
[16] H. Wu, A. Maier, R. Fahrig, J. Hornegger Spatial-temporal total variation regularization (STTVR) for 4D-CT reconstruction, *Proc. SPIE 8313* (2012), 237–240.
[17] L. Ritschl, S. Sawall, M. Knaup, A. Hess and M. Kachelrieß Iterative 4D cardiac micro-CT image reconstruction using an adaptive spatio-temporal sparsity prior, *Phys Med. Biol.*, **57(6)** (2012), 1517–1526.
[18] H. Gao, J-F. Cai, Z. Shen and H. Zhao Robust principal component analysis-based four-dimensional computed tomography, *Phys Med. Biol.*, **56(11)** (2011), 3181–3198.
[19] M. Strobl, I. Manke, N. Kardjilov, A. Hilger, M. Dawson and J. Banhart Advances in neutron radiography and tomography, *J. Phys. D: Appl. Phys.*, **42(24)** (2009), 1–21.
[20] A. P. Kaestner, S. Hartmann, G. Kuhne, G. Frei, C. Grunzweig, L. Josic, F. Schmid and E. H. Lehmann The ICON beamline - a facility for cold neutron imaging at SINQ, *Nuclear Instruments and Methods in Physics Research*, **659(1)** (2011), 387–393.
[21] K. S. Brown, S. Schluter, A. Sheppard and D. Wildenschild On the challenges of measuring interfacial characteristics of three-phase fluid flow with x-ray microtomography, *Journal of microscopy*, **253(3)** (2014), 171–182.
[22] S.Z. Li *Markov random field modeling in image analysis*, Springer, 2009.
[23] P.L. Combettes and J.C. Pesquet Proximal splitting methods in signal processing, in *Fixed-Point Algorithms for Inverse Problems in Science and Engineering*, Springer Science Business Media (2011), 1850212.
[24] D. Kazantsev, S.R. Arridge, S. Pedemonte, A. Bousse, K. Erlandsson, B.F. Hutton and S. Ourselin An anatomically driven anisotropic diffusion filtering method for 3D SPECT reconstruction, *Phys Med. Biol.*, **57(12)** (2012), 3793–3810.
[25] J. Nocedal and S. Wright *Numerical Optimization*, Springer, 2006.
[26] K. Perlin Improving noise, *ACM T. Graphic.*, **21(3)** (2002), 681–682.
[27] J. Kaipio and E. Somersalo Statistical inverse problems: discretization, model reduction and inverse crimes, *Journal of Computational and Applied Mathematics*, **198(2)** (2007), 493–504.
[28] 2D-3D PB regularization package (open-source code)
[29] A.P. Kaestner, B. Muench, P. Trtik and L.G. Butler Spatio-temporal computed tomography of dynamic processes, *SPIE Optical Engineering*, **50(12)** (2011), 1–10.
[30] T. Kohler A projection access scheme for iterative reconstruction based on the golden section, *IEEE Symposium Conference Record Nuclear Science 2004* (2004), 3961–3965.
[31] W. J. Palenstijn, K.J. Batenburg and J. Sijbers Performance improvements for iterative electron tomography reconstruction using graphics processing units (GPUs), *J. of Struct. Biol.*, **176(2)** (2011), 250–253.
[32] W.M. Thompson, W.R. Lionheart and E.J. Morton Real-Time Imaging with a high speed X-Ray CT system, *In Proc. 6th International Symposium on Process Tomography*, (2012).

Received xxxx 20xx; revised xxxx 20xx.

E-mail address: daniil.kazantsev@manchester.ac.uk
E-mail address: William.Thompson-2@manchester.ac.uk
E-mail address: bill.lionheart@manchester.ac.uk
E-mail address: geert.vaneyndhoven@uantwerpen.be
E-mail address: anders.kaestner@psi.ch
E-mail address: kate.dobson@manchester.ac.uk
E-mail address: p.j.withers@manchester.ac.uk
E-mail address: peter.lee@manchester.ac.uk